P 1.7 USING DOPPLER VELOCITY SPECTRA TO STUDY THE FORMATION AND EVOLUTION OF ICE IN A MULTILAYER MIXED-PHASE CLOUD SYSTEM

M. Rambukkange* and J. Verlinde
Penn State University

1. INTRODUCTION

Mixed-phase stratus clouds have been receiving increased attention by the polar research community over the years because of their important contribution to the energy balance of the Arctic surface. The accurate determination of this energy balance requires the correct partitioning of the two phases of water in these clouds. However, factors that govern the formation and the evolution of the two phases in these clouds are poorly understood. Therefore, to bridge some of these gaps in the knowledge about mixed-phase (MP) cloud life cycle the Atmospheric Radiation Measurement (ARM) program conducted the Mixed-Phase Arctic Cloud Experiment (M-PACE). Analyses of the M-PACE data and utilizing the data in numerical models have furthered the theoretical understanding about these clouds.

Unfortunately, most of the attention up to now has been on single layer MP clouds, so there is a dearth of knowledge about common multilayer MP clouds. At least part of this neglect of multilayer clouds can be attributed to difficulty in collecting cloud microphysical data under conditions with several cloud layers. For example, passive radiometric instruments give only vertically integrated cloud properties and lower liquid layers occult the lidar. Though the millimeter cloud radar (MMCR) Doppler radar can penetrate a wide variety of clouds, their moments alone are insufficient to separate cloud phase needed for the retrieval of cloud microphysical profiles.

We demonstrate the use of full Doppler velocity spectra collected by the ARM MMCR at Barrow, Alaska during M-PACE to separate the two phases of multilayer MP clouds, derive cloud microphysical properties and attempt to tie it to the cloud dynamics.

* *Corresponding author address*: Mahlon Rambukkange, Penn State University, Department of Meteorology, 603 Walker Building, University Park, PA 16802.
Email: mpr191@psu.edu

2. DATA AND CASE OVERVIEW

A high-pressure system located over the ocean north of Barrow, Alaska, dominated the weather over the North Slope of Alaska (NSA) during October 4-8. A weak disturbance that originated over the Eastern Brooks Range first moved westward along the North Slope coastline and then backtracked eastward before dissipating in the general area of Deadhorse. Although the low-pressure system did not cause much change in the surface winds and temperature fields, it carried sufficient moisture at mid and upper-levels to cause extensive cloudiness over the NSA. These upper-level clouds along with the boundary layer stratus caused the multilayer decks that were seen over Barrow during October 6 (Yannuzzi, 2007).

Figure 1 displays the thermodynamic and wind profiles at 10:59 UTC on October 6. The relative humidity over ice and water (RH and RH_i) are greater than 95% and 100% for the layer between 0.6 and 1.9 km; above this deep moist layer the relative humidity drops off, but a few thin layers of higher RH_i are still evident. The u and v-velocity profiles show evidence of gravity wave activity in the 1- 2 km height range.

Figure 2 depicts profiles of the MMCR and the Arctic High Spectral Resolution Lidar depolarization (HSRL, Eloranta 2007). These plots reveal the complicated multilayer structure of clouds over the site. Even a trained eye can have difficulty in identifying liquid layers in the radar reflectivity, whereas high lidar backscatter combined with low depolarization values easily reveal embedded liquid clouds. The time-height cross section of HSRL depolarization show many patches of low depolarization surrounded by higher depolarization values, which we interpret as liquid clouds embedded in ice precipitation. Unfortunately, above 2 km the HSRL is completely attenuated; hence, an alternate method to identify liquid clouds under multilayer cloud situations would be a great asset.

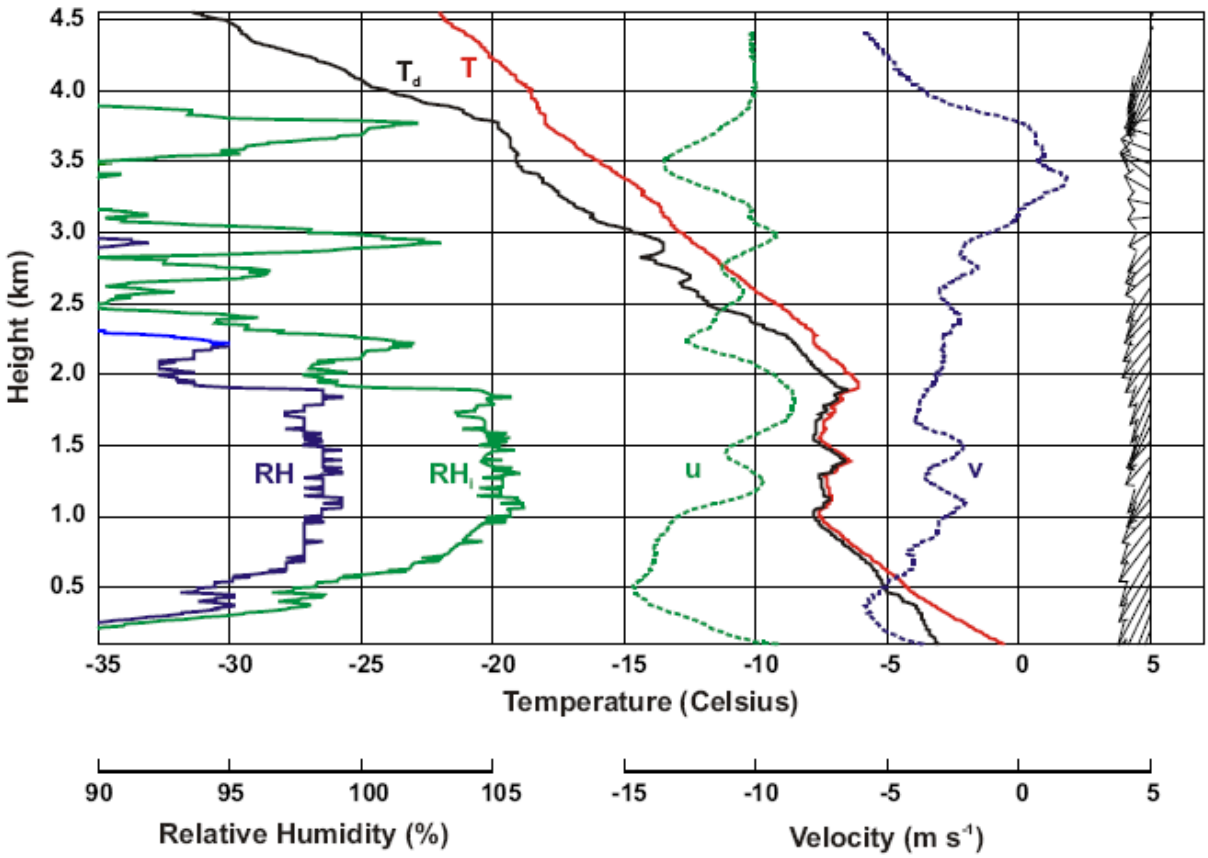

Figure 1: The thermodynamic and wind profiles from Barrow at 10:59 UTC on 6 October 2004. The red and black lines indicate temperature and dew point temperature while RH and RH_i are in green and blue with relative humidity values indicated below. The u and v wind profiles are in green and blue dashed lines and their scale is give next to the axis used for relative humidity. The black arrows show profiles of the resultant of u and v wind components.

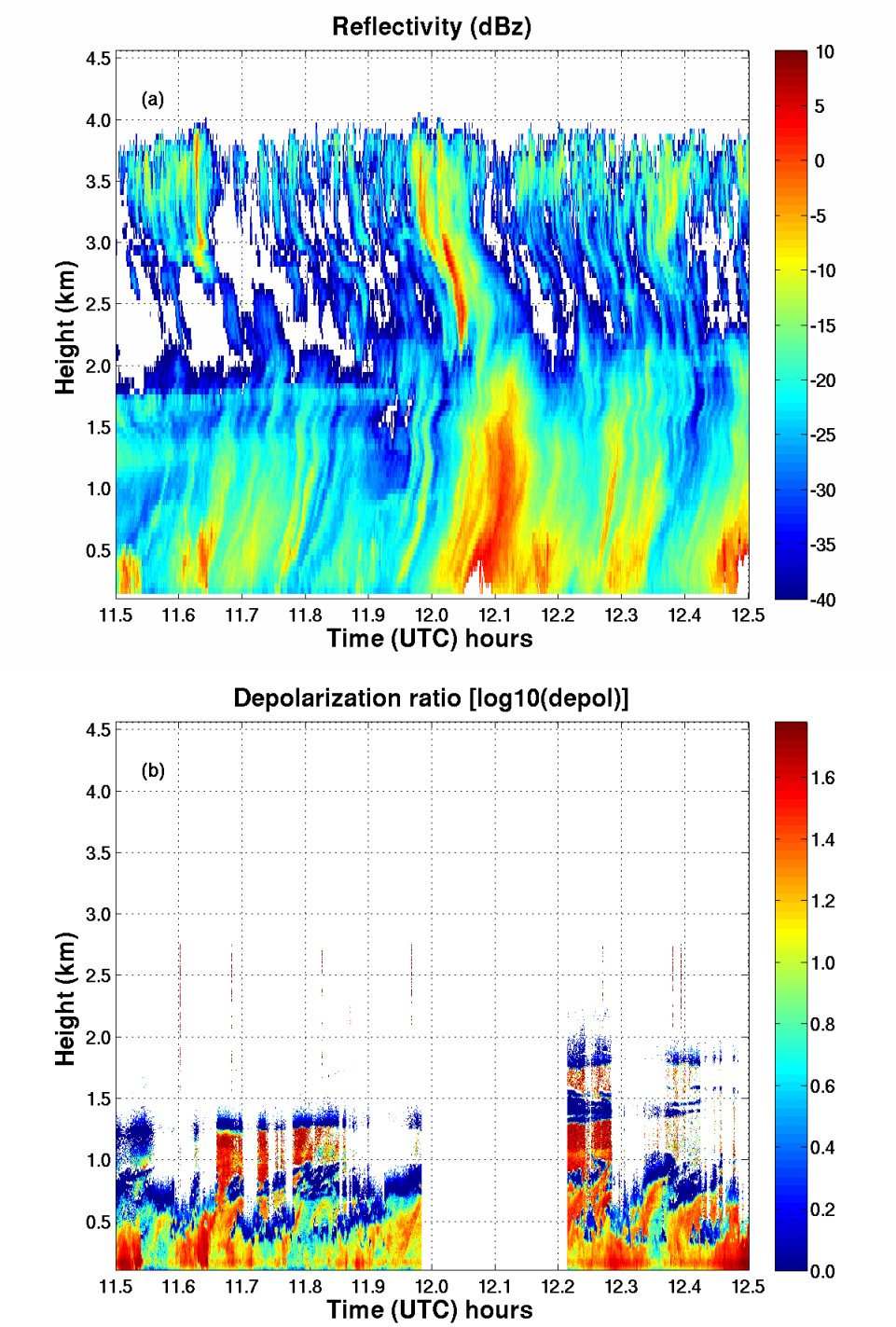

Figure 2: (a) time-height plot of reflectivity (dBZ) from the Millimeter Wave Cloud Radar (MMCR). (b) time-height cross section of depolarization ratio (log10 [depolarization]) from the High Spectral resolution Lidar (HSRL) located at Barrow.

3. DOPPLER VELOCITY SPECTRA

The most common measurements obtained from a Doppler radar are reflectivity, mean Doppler velocity and spectrum width. These measurements are the lowest moments of the full Doppler spectrum: the zeroth moment (radar reflectivity), the first moment (mean Doppler velocity), and the second moment (spectrum width). The Doppler velocity spectrum is the backscattered power distributed as function of the radial velocity. Saving the full Doppler spectra requires a large amount of data storage space, so usually the moments are recorded and the Doppler spectrum is discarded. However, the Department of Energy (DOE) Atmospheric Radiation Measurement (ARM) program records both the moments and the full Doppler spectra. The Doppler spectrum contains more information about the hydrometeors in the radar sample volume than its three moments. In this study, we will use the full Doppler spectrum.

Figure 3 depicts a cleaned and calibrated Doppler spectrum obtained from our analysis period. By convention, hydrometeors moving away from the vertically pointing radar have negative velocities. In figure 3, we see that the power returns from hydrometeors have two separate velocity ranges. For this discussion, we will refer to the spectral peak left of the zero-velocity as A and the other as B. The large velocity separation of 0.5 m s^{-1} between A and B suggests that they are two distinct hydrometer distributions. The hydrometeors in A move upward with velocities close to 0.1 m s^{-1} while the stronger spectral peak B contains hydrometeors that fall down with velocities between 0.5 – 1.0 m s^{-1}. Cloud particles (10 – 20 μm) have velocities of about 1- 20 cm s^{-1}, whereas the typical fall speeds of ice precipitation for the M-PACE Arctic stratus are around 1.0 m s^{-1}, which is close to the highest velocity in B. Hence, one may suggest a preliminary distinction between these two distributions; i.e., A and B correspond to cloud and ice precipitation distributions, respectively. The integrated spectral reflectivities for A (-29 dBZ) and B (-23 dBZ) supports this inference; the reflectivity of A is close to that of a cloud, whereas that of B could represent light precipitation.

The reflectivity and velocity information from the spectrum are insufficient to determine the phase of the cloud particles. With additional information from the HSRL that measured low depolarization (1.2%) and high lidar backscatter in the same volume, we conclude that peak A corresponds to a cloud droplet distribution.

Lower liquid layers in our multilayer MP cloud case (Fig. 2a and 2b) blocks the HSRL, so we seek for an alternate method to find locations of higher liquid layers. Analyses of Doppler spectra from our multilayer clouds case reveal that a significant fraction of these spectra contains clear bimodality (as in Fig. 3) when the HSRL detected liquid. In such cases the slowest particle fall speed, which is the first spectral point from the left, gives (to a good approximation) the radar volume mean air velocity. Fig. 4 depicts the time-height cross section of slowest hydrometeor velocity. The plot demonstrates sharp jumps in the velocity at boundaries between liquid clouds and ice precipitation, which can be used to identify locations of clouds. In Fig. 4, we can see clouds up to the reflectivity top (Fig. 2a). Comparing Fig. 2b and Fig. 4, at heights where the HSRL is not attenuated the cloud locations derived from the slowest hydrometeor velocity are in good agreement with cloud locations detected by the HSRL.

The Doppler power spectra recorded by the ARM program are a function of time, height velocity, which makes the spectra a four dimensional data set. This makes visualization of Doppler spectra to identify and interpret cloud processes a challenge. We use two methods to visualize Doppler spectra. First, we construct a spectrograph by combining spectra at an instant in time (profile-spectrograph). In this case, a spectrograph is a topographical map of spectral power as a function of velocity and height. We can also construct a spectrograph from a time series of spectra collected at a particular height: for distinction, we define this as a time-series spectrograph.

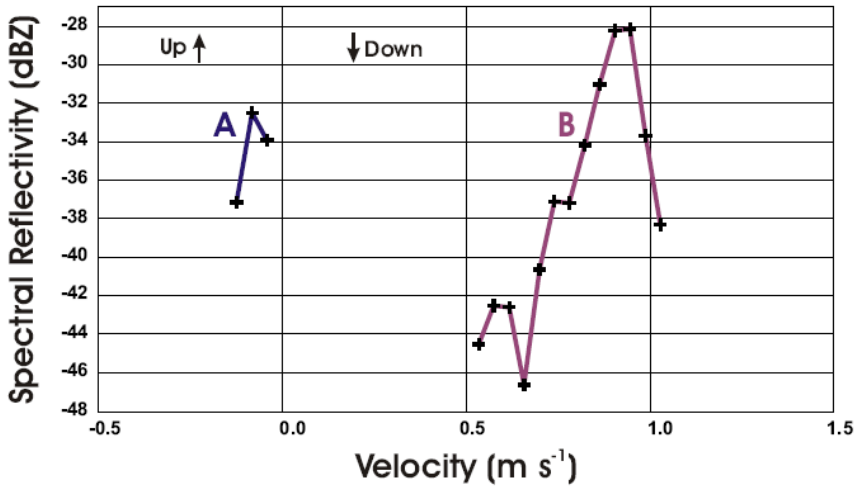

Figure 3: a calibrated Doppler spectrum from height 1.86 km and time 12.26 hours (UTC) on 6 October 2004. The spectrum contains two spectral peaks corresponding to two distinct hydrometeor populations indicated by A and B.

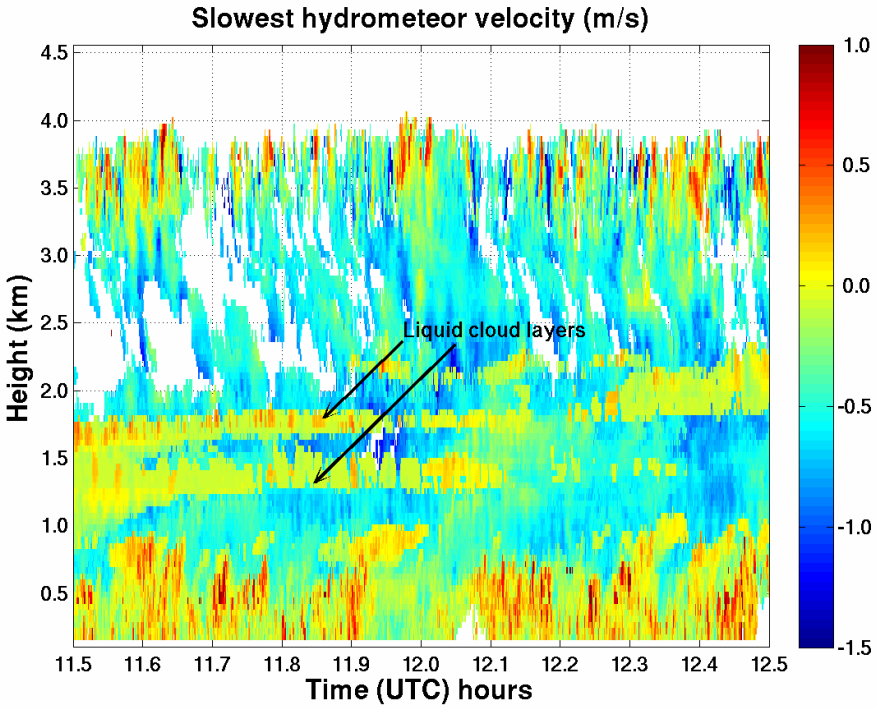

Figure 4: time-height plot of slowest hydrometeor fall velocity for the same heights and times as in Fig. 2.

Figure 5 illustrates the construction of a profile-spectrograph. The profile-spectrograph in Fig. 5b was obtained at a time when the HSRL detected a layer with low depolarization and high lidar backscatter at 1.9 km. Therefore, we indicate this liquid layer by 'cloud' on the profile-spectrograph.

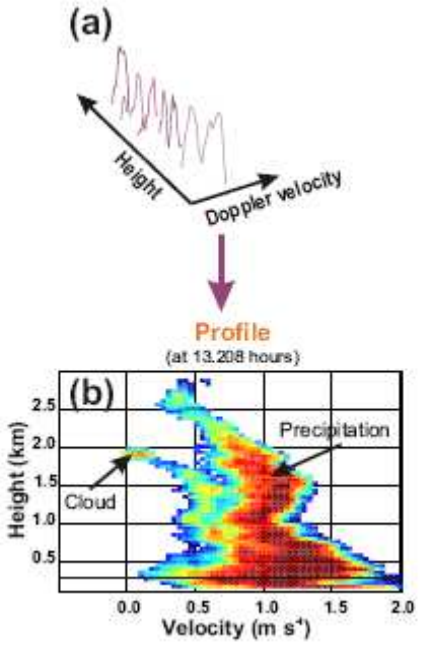

Figure 5: (a) illustrates Doppler spectra are stacked as a function of height and velocity. (b) shows a topographic map of spectra that were stacked in (a), which we shall call a profile-spectrograph.

3.1 *Using Velocity Spectra to Partition Reflectivity*

Figure 6 depicts the profile-spectrograph obtained at 12.09 UTC. With the aid of the slowest hydrometeor velocity (Fig. 4), we identify three embedded liquid layers, which are indicted by the orange ovals: for distinction, we name them 'Top', 'Mid', and 'Bot' cloud. Therefore, the remaining spectral points above 0.75 km correspond to ice precipitation (see Fig. 2). A closer look at the ice precipitation below the liquid layers reveals that distinct modes of ice may extend up to these liquid layers. Analyses of spectra between 12.00 and 13.00 UTC confirms that the ice does in fact extend up to these liquid layers. In addition, spectral points with velocities comparable to the liquid droplets are not present above these liquid layers, so we conclude that what we observe is ice falling out of these liquid layers. Fig. 5b shows a clear example of ice falling out the liquid layer at 2.0 km.

To quantify liquid and ice, we use a semi-automated method to separate liquid from ice: '0's indicate the demarcation between liquid and ice. After removing spectral points of the liquid cloud, we trace valleys (local minima) in the remaining portion of the profile-spectrograph (a topographic map) to separate ice populations depending on their origin: i.e., whether they formed within 'Top', 'Mid', 'Bot' cloud or above 'Top' cloud. Valleys traced out in this manner are indicated by '1's,'2's, and '3's in Fig. 6. We employ these valleys to group spectral points into four populations (classes) of ice and use the points in each group to obtain the zeroth and first moment of each ice population. For the droplet distribution, the zeroth moment is computed in a similar manner to the ice, but instead of the first moment, the slowest hydrometer velocity is obtained because it gives air motions within cloud. We will refer to the zeroth moment of liquid and four ice populations obtained according to this method as the reflectivity partitions.

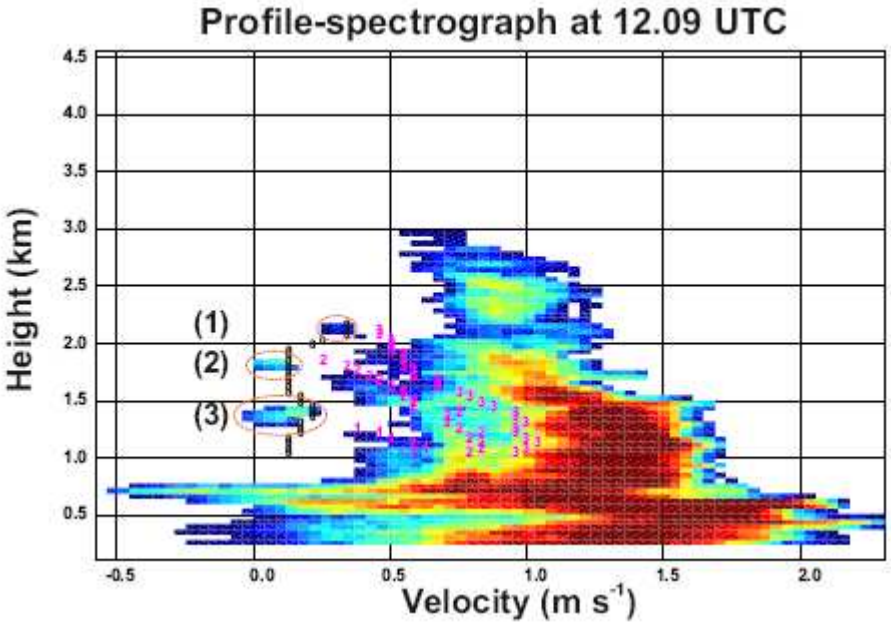

Figure 6: depicts the profile-spectrograph at 12.09 UTC. The symbols '0','1','2' and '3' illustrate where the profile –spectrograph is divided to obtain reflectivity partitions. Top liquid cloud ('Top'), Bottom liquid cloud ('Bot'), and Middle liquid cloud ('Mid') are three liquid layers used for this study.

4. RESULTS

Figure 7 is a depiction of our idealized conceptual model of three liquid layers (Fig. 6) embedded in ice precipitation. In Fig. 2, we observed precipitation formed in higher clouds (e.g., clouds at 3.9 km); in the schematic, the precipitation entering the 'Top' cloud is indicated by "1-IN-A". Here '1-IN' refers entering the Top cloud and A indicates that the ice was formed above the 'Top' cloud. Similarly, ice crystals formed in 'Top', 'Mid', and 'Bot' are indicated by '1-B-OUT', '2-C-OUT', and '3-D-OUT', respectively.

Figure 8 depicts the time-height cross sections of reflectivity partitions. The blue and red arrows show the partition of total reflectivity between 12.00 and 12.13 UTC into ice and liquid water using Doppler spectra. The symbols '1', '2' and '3' in the liquid reflectivity plot indicate 'Top', 'Mid' and 'Bot' shown in the schematic. After separating ice from liquid, the ice is further divided into four parts (A, B, C and D): here A, B, C, and D represent the reflectivities of four ice populations (see Fig. 6 and Fig. 7).

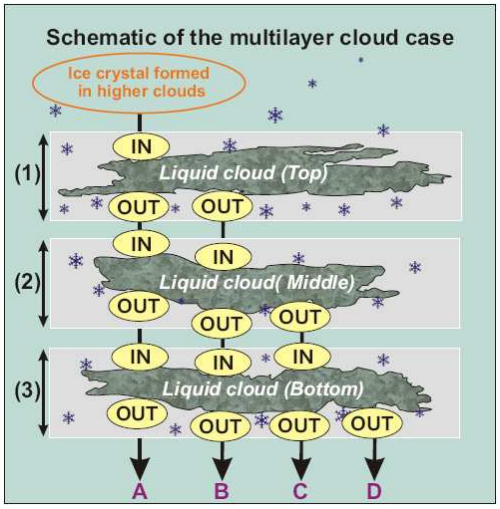

Figure 7: illustrates how properties of ice formed within the three liquid clouds ('Top', 'Mid' and 'Bot') and above "Top' clouds are tracked as a function of height.

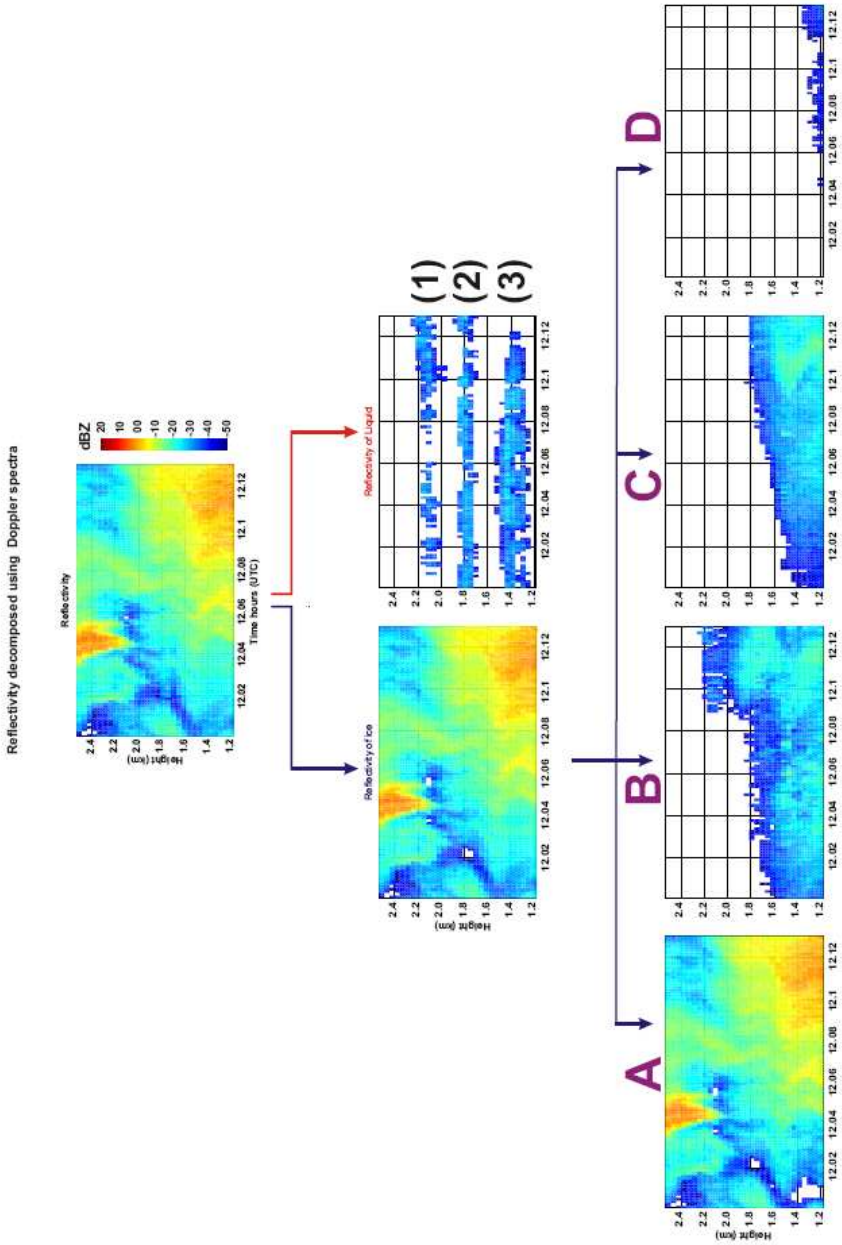

Figure 8: shows the separate contributions to reflectivity from the ice and liquid. The ice is partitioned into four components (A, B, C and D) using Doppler spectra.

We employ methods described in Frisch et al. 1994 and Shupe et al. 2008 to obtain cloud LWC and IWC from the partitioned reflectivities. Figure 9a shows profiles of time averaged reflectivity for the three cloud layers ('1','2', and'3') and four ice populations while Fig. 9b depicts the LWC and IWC profiles for these liquid layers and ice. For clarity, numbers indicated in the boxes on the top of each figure were used to scale the reflectivity and IWCs. In general, the reflectivity increases as the precipitation descend to 1.2 km; however, distinct changes in the slope are seen as ice passes through each liquid layer. A notable exception is the rapid reflectivity decrease in the black line above 2.0 km, which resulted from a highly reflective shower only descending to about 2 km at the time of the observation (12.05 UTC Fig. 2a).

The layer between 1.2-1.9 km is supersaturated with respect to ice (Fig.1). Hence, one may expect three microphysical processes to contribute to the increase in reflectivity. They are vapor depositional growth (faster in liquid layers), riming (only in liquid layer) and aggregation (everywhere). Although vapor growth and riming increases the size of ice crystals aggregation is expected to have the biggest impact on the size and hence the reflectivity (or IWC). In contrast, the particle velocities decrease in aggregates (reduces bulk density) and riming tends to increase the velocity by increasing the particle bulk density. All three processes contribute to the increase of reflectivity, so it is difficult to isolate their relative contributions to the change in slope within liquid layers.

In order to determine cause of the change in slope we computed the mean fall speeds of each population (Fig. 9c). To obtain fall velocities of each population with respect to still air we subtracted an estimated volume mean (vertical) motion from the population mean vertical motions. The air motions at all heights were determined by interpolating the slowest hydrometeor fall velocity (Fig. 4) over the gaps between cloud layers.

Fig. 9c shows time-averaged velocities of the smallest cloud droplets in red and the quiet air fall speeds of the four populations of precipitation in blue, green, cyan, and black. We observe a sharp increase in fall velocity when the populations enter the clouds and reach the maximum liquid water content after which the fall-speed increase slows down. The increased fall speeds near cloud top is consistent with growth dominated by riming. However, at this point we cannot explain the slowing down of the rate of increase in the velocity near the bottom of liquid layers before it picks up again close to cloud base.

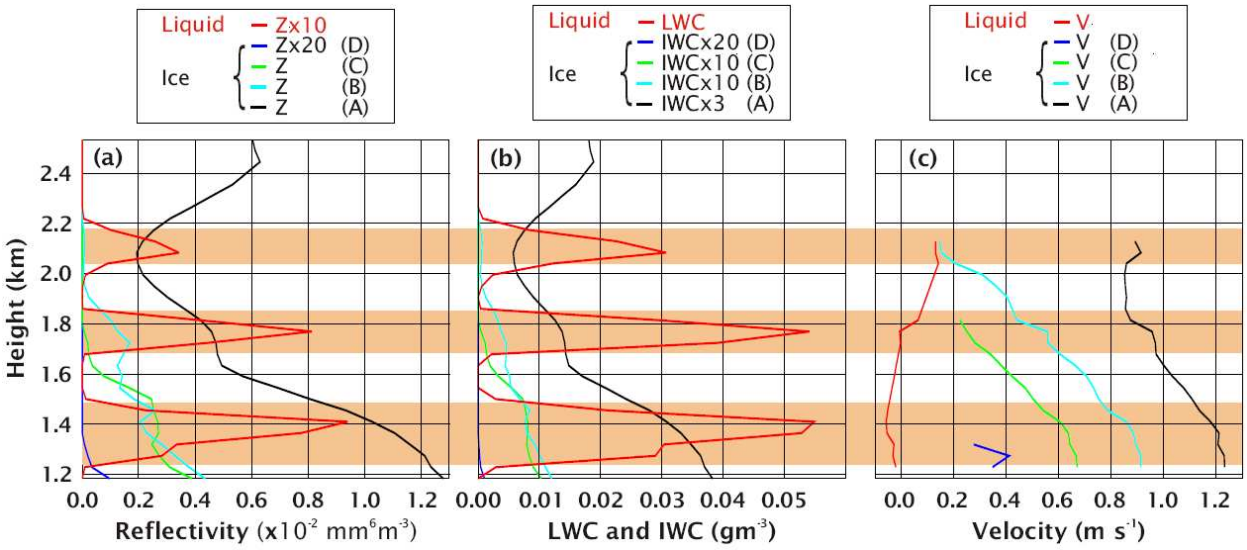

Figure 9: (a) reflectivity profiles of the three cloud layers ('1','2', and '3') and four ice populations (A, B, C and D). (b) LWC and IWC of the liquid layers and ice populations (c) the velocity profile of the cloud layers and quiet air fall speeds of A, B, C and D.

5. CONCLUSION

We demonstrate the use of the HSRL and slowest hydrometeor velocity obtained from Doppler spectra at times when spectra display clear bimodality to obtain locations of liquid clouds that are undetected by HSRL. We document the use of Doppler spectra to separate out the contributions from liquid and ice to radar reflectivity and further partition reflectivity of the ice into different populations. From these partitioned reflectivities, we compute cloud properties and obtain profiles of LWC, IWC and velocity.

Our preliminary results demonstrate how ice showers entering and exiting the radar line of sight probably caused by wind shear complicates the analyses of cloud properties. In addition, as ice formed in higher clouds fall through cloud layers at lower heights they undergo significant changes in their reflectivity and velocity, which are caused by modifications to their shape, size, and number. In order to have better grasp of the ice processes and interpret our results we will increase the analyses period to over an hour and estimate growth rates of ice crystals by vapor growth and riming.

6. REFERENCES

Babb, D.M., J. Verlinde, and B. A. Albrecht, 1999: Retrieval of Cloud Microphysical Parameters from 94-GHz Radar Doppler Power Spectra. J. Atmos. Oceanic Technol., 16, 489–503.

Curry, J.A. and G. F. Herman, 1985: Infrared radiative properties of Arctic stratus clouds. J. Clim. Appl. Met., 24, 525-538.

Eloranta, E.W., T. Uttal and M.D. Shupe 2007: Cloud particle size measurements in Arctic clouds using lidar and radar data. IEEE Trans. Geosci. Remote Sens., 23-28, 2265-2267.

Frisch, A.S., C.W. Fairall, and J.B. Snider, 1995: Measurement of Stratus Cloud and Drizzle Parameter in ASTEX with a K□- Band Doppler Radar and a Microwave Radiometer. J. Atmos. Sci. 52, 2788-2799.

Frisch, A.S., M.D. Shupe, I. Djalalova, G. Feingold, and M.R. Poellot, 2002:
The Retrieval of Stratus Cloud Droplet Effective Radius with Cloud Radars. J. Atmos. Oceanic Technol., 19, 835–842.

Gossard, E.E., J. B. Snider, E. E. Clothiaux, B.E. Martner J.S. Gibson, R. A. Kropfli, and A.S. Frisch, 1997: The Potential of 8-mm Radars for Remotely Sensing Cloud Drop Size Distributions. J. Atmos. Oceanic Technol. Sci., 14, 76–87.

Herman, G.F., and R.M. Goody, 1976: Formation and persistence of summertime Arctic stratus clouds, J. Atmos. Sci., 33, 1537-1553.

McFarquhar, G. M., and S. G. Cober, 2004: Single-Scattering Properties of Mixed-Phase Arctic Clouds at Solar Wavelengths: Impacts on Radiative Transfer. J. Climate, 17, 3799–3813.

Pinto, J. O., 1998: Autumnal mixed-phase cloudy boundary layers in the Arctic. J. Atmos. Sci., 55, 2016-2038.

Shupe, M.D., T. Uttal, and S.Y. Matrosov, 2005: Arctic Cloud Microphysics Retrievals from Surface-Based Remote Sensors at SHEBA. J. Appl. Meteor., 44, 1544-1562.

Shupe, M. D., and S.Y. Matrosov, 2006: Arctic mixed-phase cloud properties derived from surface-based sensors at SHEBA. J. Atmos. Sci., 63, 697-711.

Shupe, M.D., and P. Kollias, P. Ola G. Persson, G. M. McFarquhar, 2008 a: Vertical Motions in Arctic Mixed-Phase Stratiform Clouds. J. Atmos. Sci., 65, 1304–1322.

Shupe, M.D., and P. Kollias, M.R. Poellot, E. Eloranta, 2008 b: On Deriving Vertical Air Motions from Cloud Radar Doppler Spectra. J. Atmos. Oceanic Technol Sci., 25, 547–557.

Sun, Z., and K.P. Shine, 1994: Studies of the radiative properties of ice and mixed-phase clouds. Quart. J. Roy. Meteorol. Soc., 120, pp. 111-137.

Verlinde, J., and others, 2007: The mixed-phase Arctic cloud experiment. Bull. Amer. Meteor. Soc., 88, 205-221.

Yannuzzi, V.T., 2007: A Statistical Comparison of Forecasting Models across the North Slope of Alaska during the Mixed-Phase Arctic Cloud Experiment. M.S. thesis, Penn State University, UP.